Supplementary Information

Deciphering the intracellular forces shaping mitochondrial motion

Agustina Belén Fernández Casafuz[1,+], Azul María Brigante[2], María Cecilia De Rossi [3,5] , Alejandro Gabriel Monastra[4,5] and Luciana Bruno[1,5,*]

[1]CONICET - Universidad de Buenos Aires, Facultad de Ciencias Exactas y Naturales, Instituto de Cálculo (IC). Buenos Aires, 1428, Argentina
[2]Universidad de Buenos Aires, Facultad de Ciencias Exactas y Naturales, Departamento de Física. Buenos Aires, 1428, Argentina
[3]CONICET - Universidad de Buenos Aires, Facultad de Ciencias Exactas y Naturales, Departamento de Química Biológica, Instituto de Química Biológica (IQUIBICEN). Buenos Aires, 1428, Argentina
[4]Universidad Nacional de General Sarmiento, Instituto de Ciencias. Los Polvorines, 1613, Argentina
[5]Consejo Nacional de Investigaciones Científicas y Técnicas (CONICET), Argentina

+afcasafuz@ic.fcen.uba.ar
*lucianabrun@gmail.com

The Supplementary information contains the following Sections:

1. Numerical model of mitochondria and simulations

Before describing the conducted simulations, we must make a disclaimer: our model is very simple as it considers a 1D filament in a pure viscous medium, which clearly deviates from the conditions of mitochondria immersed in the cytoplasm. However, our goal is to explore and quantify the effects of non-thermal kicks on a semiflexible filament with mechanical characteristics similar to those of mitochondria. Therefore, we decided to use a simple model as a first approximation to the real biological system.

We considered the Worm-Like Chain model[1], as was described in Monastra et al[2].

The filament is divided into N equal segments of length $\Delta L = L/N$. The configuration is determined by the (N + 1) coordinates, $\mathbf{r}_n$, of the endpoints of each segment, where $0 \leq n \leq N$, so-called beads. In terms of these coordinates, elastic and bending potential energies are written as:

$$V_{\mathrm{E}} = \frac{1}{2}\frac{EA}{\Delta L}\sum_{n=0}^{N-1}\left(|\mathbf{r}_{n+1}-\mathbf{r}_n|-\Delta L\right)^2$$

$$V_{\mathrm{B}} = \frac{EI}{\Delta L}\sum_{n=1}^{N-1}\left[1-\frac{(\mathbf{r}_{n+1}-\mathbf{r}_n)\cdot(\mathbf{r}_n-\mathbf{r}_{n-1})}{|\mathbf{r}_{n+1}-\mathbf{r}_n|\,|\mathbf{r}_n-\mathbf{r}_{n-1}|}\right]$$

where E is the Young modulus, A is the transverse area of the filament and I is the second moment of area. The product EI is also called the flexural rigidity of a beam. In the limit $\Delta L \to 0$ these expressions tend to continuous elastic and bending energies in terms of strain and curvature of the filament, respectively. Deriving the potential energies with respect to the coordinate $\mathbf{r}_n$, elastic and bending forces are obtained,

$$\mathbf{F}_n^{\mathrm{E}} = -\frac{\partial V_{\mathrm{E}}}{\partial \mathbf{r}_n},$$

$$\mathbf{F}_n^{\mathrm{B}} = -\frac{\partial V_{\mathrm{B}}}{\partial \mathbf{r}_n},$$

which are applied to the corresponding bead n.

The viscous force is given by,

$$\mathbf{F}_n^{\mathrm{vis}} = -c\, a_n\, \Delta L\, \dot{\mathbf{r}}_n$$

with a_n=1 for $1 \leq n \leq (N-1)$, and a_n=½ for the end beads $n = 0$ and $n = N$, corresponding to the drag on both ending semi-segments. The parameter c is the drag coefficient per unit length[3], expressed as:

$$c = \frac{4\pi\eta}{\ln(L/\phi)+0.84}$$

that corresponds to a cylindrical filament of length *L* and diameter ϕ, and η is the medium dynamical viscosity.

Moreover, we considered eventual external active point-like forces $\mathbf{F}^{act}$ acting on the beads. Supplementary Fig. S1 illustrates the model.

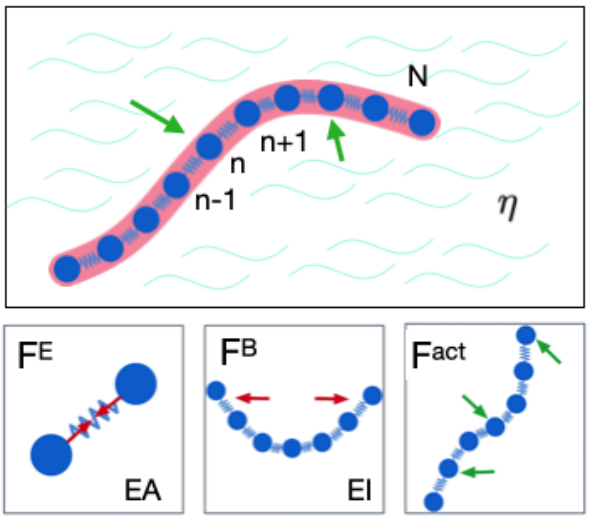

Supplementary Fig. S1. Schematic representation of a semiflexible filament in a viscous medium. F^E, F^B and F^{act} are the elastic, bending and active forces considered in the model

Neglecting the inertia of the filament, we get (*N* + 1) coupled first-order differential equations,

$$\mathbf{F}_n^{\mathrm{E}} + \mathbf{F}_n^{\mathrm{B}} + \mathbf{F}_n^{\mathrm{act}} + \mathbf{F}_n^{\mathrm{vis}} = 0$$

from where we computed the instantaneous velocity for each bead as:

$$\dot{\mathbf{r}}_n = \frac{1}{c\, a_n\, \Delta L}\left(\mathbf{F}_n^{\mathrm{E}} + \mathbf{F}_n^{\mathrm{B}} + \mathbf{F}_n^{\mathrm{act}}\right)$$

From an initial configuration of the beads (*t* = 0), and the instantaneous velocities, the new positions of the beads after a sufficiently small time interval δt can be inferred. These would be the new positions at $t = \delta t$ given by the deterministic forces. On top of this, the thermal brownian motion given by the environment produces a normal diffusion whose variance in each direction is proportional to δt [4]. Therefore, the new positions were computed as

$$\mathbf{r}_n(t+\delta t) = \mathbf{r}_n(t) + \dot{\mathbf{r}}_n(t)\ \delta t + \sqrt{\frac{2k_{\mathrm{B}}T}{c\, a_n\, \Delta L}}\,\mathbf{w}_n\sqrt{\delta t}$$

with k_B the Boltzmann constant and T the absolute temperature. Here, $\boldsymbol{w}_n$ represents a vector of independent Gaussian random numbers with zero mean and unit variance[4]. Iterating the procedure, the evolution of the filament under the action of internal (elastic, bending) and external forces (drag, active, and thermal) can be obtained. The value of δt should fulfill the following condition to converge:

$$\max(\dot{\mathbf{r}}_n)\delta t \ll \Delta L$$

The simulations of this system were carried out using a Python code developed in our group, and the parameters used in the numerical model are displayed in Supplementary Table S1. These parameter values emulate the morphological and mechanical features of mitochondria in *X. laevis* melanophores, as reported in previous studies [5,6].

Mito length (L)	2-5 μm	-
Mito diameter (ϕ)	350 nm	Ref.[5,6]
Flexural rigidity (EI)	8.10^3 pN nm^2	Ref.[5,6]
Elastic constant (EA)	1.04 pN	Ref. [5,6]
Viscosity (η)	$10^{-2} - 10^{-4}$ cP	Ref. [7]
Thermal energy ($k_B T$)	4 pN nm	-

Supplementary Table S1. Parameters used in the simulations.

Preliminary tests were conducted where the equilibrium distance between beads (ΔL) and the iteration time (δt) were adjusted to determine the values that guarantee the stability of the simulations for the different considered viscosities (see Supplementary Table S2)

η [cP]	ΔL_1 [nm]	δt_1 [s]	ΔL_2 [nm]	δt_2 [s]
10^2	50	5.10^{-9}	100	10^{-8}
10^3	50	5.10^{-8}	100	10^{-7}
10^4	50	5.10^{-7}	100	10^{-6}

Supplementary Table S2. Distance between beads and integration time step used in the simulations.

We performed simulations of semiflexible filaments starting from initial configurations that reproduced the shapes of mitochondria tracked from the microscopy images (Supplementary Fig. S2). Simulated filament shapes were saved with a sampling time Δt = 1 s, the same order of magnitude as the experimental ones.

First of all, we found that the simulations done with $\eta = 10^3$ cP better approximate the temporal evolution of experimentally recovered shapes. In the same total time, the filaments in the more viscous medium showed almost no variation, while the shapes with a medium viscosity of 10^2 cP exhibited greater mobility. Although this result cannot be generalized for every experimental tracking data, we decided to use a viscosity of 10^3 cP to explore the effects of active forces acting on the filaments.

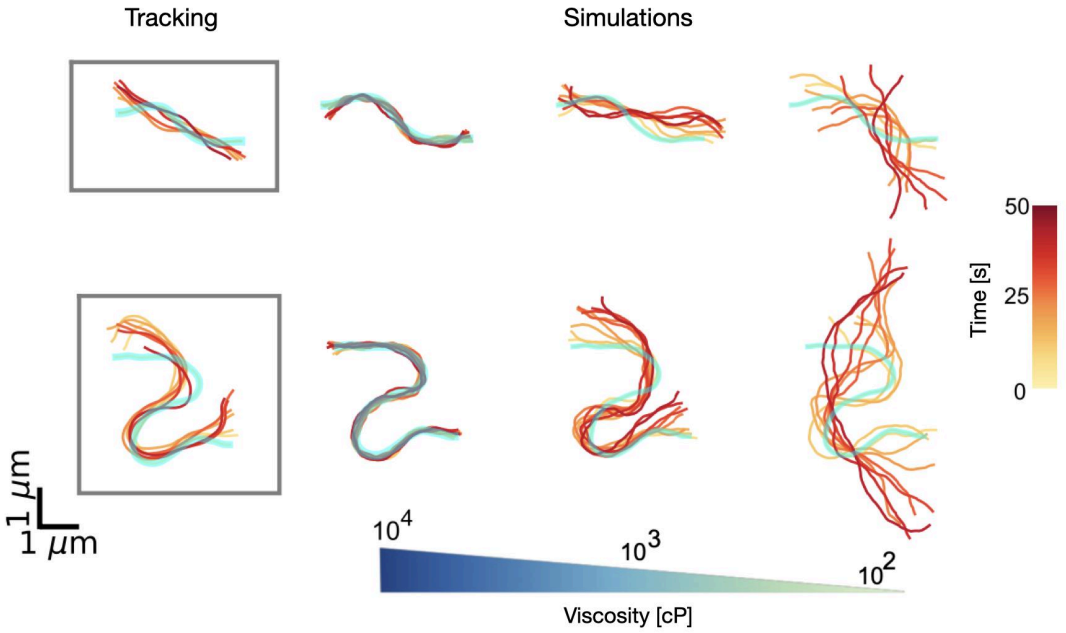

Supplementary Fig. S2. Representative simulation results. Two mitochondria shapes recovered from the tracking of mitochondria in *X. laevis* melanophores (boxes) are compared to three simulations starting from the same initial conditions (cyan curve) with viscosities: 10^2, 10^3 and 10^4 cP.

Active forces were modeled as piconewton kicks acting in aleatory directions on individual randomly chosen "active" beads (Supplementary Fig. S3). The magnitude and duration of the applied forces were sampled from Poisson distributions, with mean values of 2 pN and 3 seconds, respectively. Different force configurations, *i.e.* fraction of "active" beads, were explored and used for the analysis of the event detection algorithm's performance.

Supplementary Fig. S3. Representative simulation results with two different force patterns. The initial filament's shape was the same in both simulations (cyan curve) and viscosity was 10^3 cP. The arrow indicates the direction of the active forces.

2. Anomalous diffusion exponents and apparent diffusion coefficients within *X. laevis* melanophore cells

We used a Gaussian mixture model[8] to analyze the anomalous diffusion exponents α. This model assumes that the data are a combination of samples obtained from *M* normal

distributions with mean $\boldsymbol{\alpha}_m$ (m = 1, ..., M). The multimodal distribution $f(\alpha)$ can be expressed as:

$$f(\alpha) = \sum_{m=1}^{M} p_m \frac{1}{2\pi\sigma} e^{-\frac{1}{2}(\frac{\alpha-\alpha_m}{\sigma})^2}$$

where p_m (m = 1, ..., M) represents the relative size of the m-subpopulation with:

$$\sum_{m=1}^{M} p_m = 1$$

The center $\boldsymbol{\alpha}_m$ of each subpopulation (*i.e.* mode) is a local maximum of the density distribution. The maximum likelihood estimators of the parameters (σ, $\boldsymbol{\alpha}_m$, p_m) were obtained using the Gaussian Mixture object from the Scikit learn Mixture package `sklearn.mixture` in Python[9]. The model was selected following the Akaike information criterion[10]. The parameters' errors were computed using a bootstrap procedure.

We tested models with 1 and 2 modes. Supplementary Fig. S4 shows the kernel density of α and the models with M = 1 and 2 that better fit the data. In order to select which model described better each experimental distribution, we asked that every population fraction (for the case M = 2) was over 0.1 and that the confidence intervals of the mode's mean values did not overlap.

We found that all conditions but latrunculin-B treatment, could be well fitted by a single normal distribution (M = 1) with a mean value around α = 1. For the case of latrunculin-B treated cells, we found that a bimodal distribution (M = 2) fitted the data better, indicating the presence of two different populations, notably a significant superdiffusive one. The parameters of the chosen models are displayed in Supplementary Table S3.

Condition	μ_1	σ	f_1	μ_2	σ	f_2
CTRL	1.00 ± 0.03	0.3 ± 0.02	1	-	-	-
NOC	0.96 ± 0.04	0.3 ± 0.02	1	-	-	-
LAT	0.76 ± 0.05 *	0.4 ± 0.01	0.46 ± 0.07	1.36 ± 0.06 *	0.4 ± 0.01	0.54 ± 0.07
VIM$^-$	0.84 ± 0.04 *	0.3 ± 0.02	1	-	-	-

Supplementary Table S3. Gaussian mixture model parameters. μ_m and σ correspond to the mean position and standard deviation of gaussian m, respectively. f_m is the fraction representing the contribution of gaussian m to the overall distribution. Errors were computed following a bootstrap procedure with 100 repetitions. Asterisks denote significant differences (p-value < 0.05) between data sets and control condition, as described in Methods.

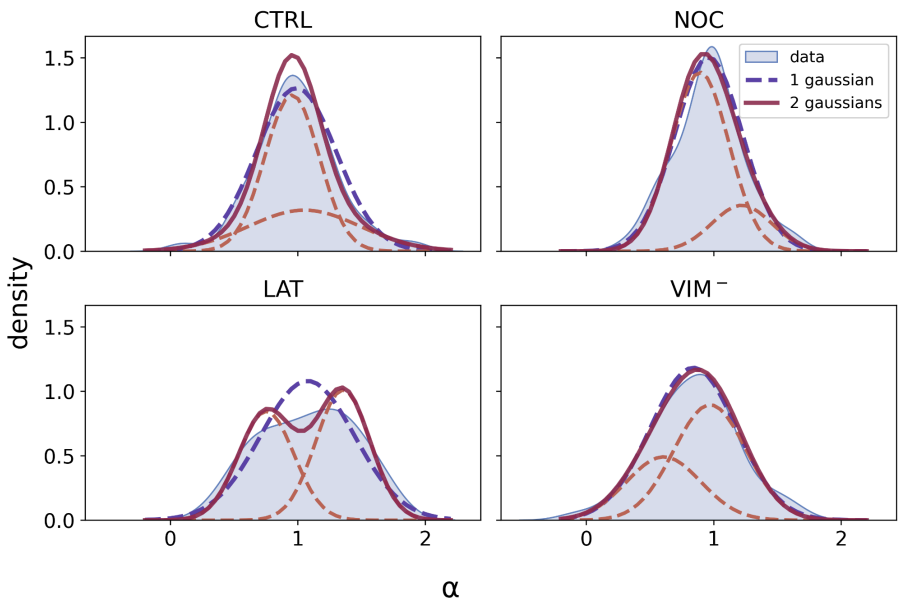

Supplementary Fig. S4. Anomalous diffusion exponent (α) distribution. The exponents obtained for each experimental condition (light blue) were quantitatively analyzed as described above considering a mixture of Gaussian functions with one (violet dashed) or two modes (solid bordeaux and dashed orange lines).

We also determined the apparent diffusion coefficients as the *D** values whose corresponding $\alpha \simeq 1$, as shown in Supplementary Fig. S5 and Supplementary Table S4.

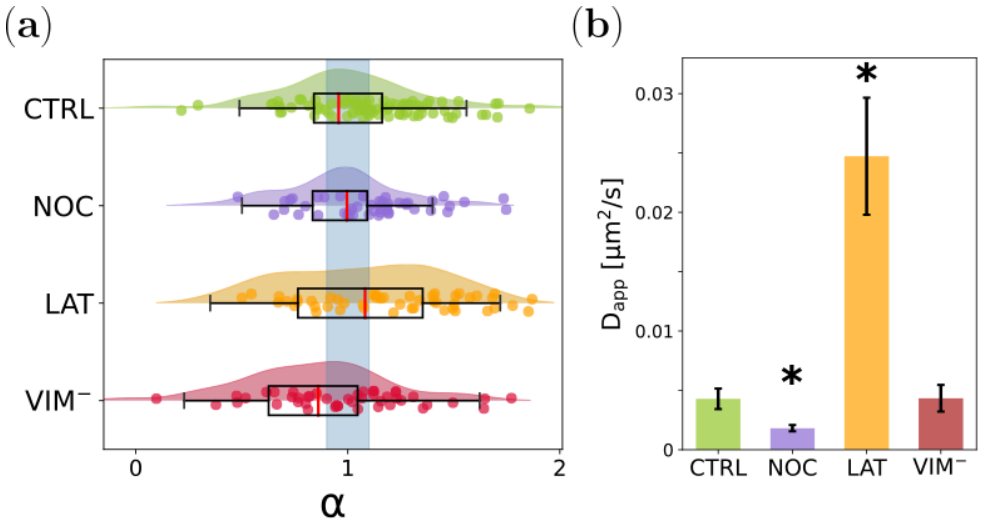

Supplementary Fig. S5. Determination of apparent diffusion coefficients (D_{app}). For each experimental condition, D_{app} were determined as the *D** values whose corresponding $\alpha \simeq 1$, as indicated by the light blue box in (a). Asterisks denote significant differences (p-value < 0.05).

Condition	$D_{app}\ 10^{-4}(\mu m^2/s)$	N
CTRL	43 ± 8	27
NOC	18 ± 3 *	18
LAT	250 ± 50 *	9
VIM^-	40 ± 10	12

Supplementary Table S4. Apparent diffusion coefficient. Asterisks denote significant differences (p-value<0.05) between data sets and control condition, as described in Methods. N is the number of data considered for each condition.

3. Events detection in the CSD data

As discussed in the manuscript, events in the CSD plots correspond to outliers in the *K* distribution. However, a single event can be associated with multiple outliers. We developed an algorithm to automatically detect extreme values from the *K* data, and define single events based on a clustering criterion applied to these data.

a. Outliers detection from *K* data

We started from a discrete description of the filament, composed of N_b material points, whose x_b and y_b coordinates at different times t are obtained either through tracking or as a result of numerical simulations.

We computed $K(t)$ using the following equation:

$$K(t) = 1/N_b \sum_{b=1}^{N_b} [(x_b[t + \Delta t] - x_b[t])^2 + (y_b[t + \Delta t] - y_b[t])^2]$$

where Δt is the sampling time (typically Δt = 1 s).

According to the simulations discussed in the first section, the distribution of *K*(t) is expected to fluctuate around a stationary value in the absence of active forces, due to thermal agitation. However, if the filament receives a significant kick, extreme values of *K* - *i.e*. *K**- will appear in the distribution (Supplementary Fig. S6).

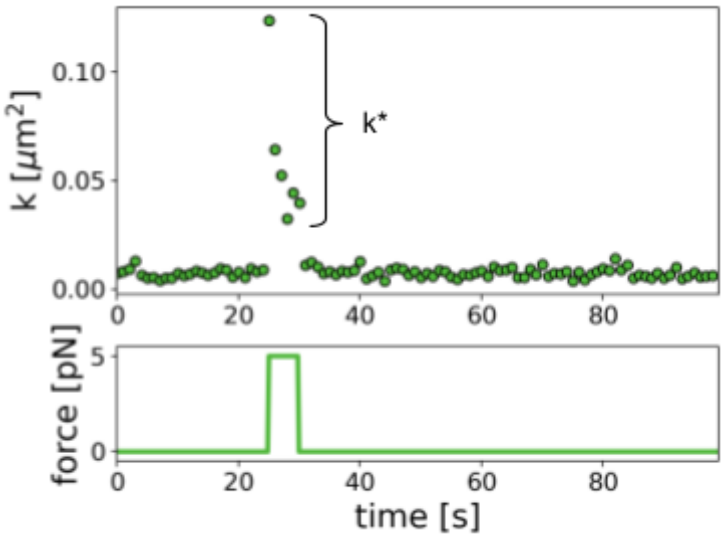

Supplementary Fig. S6: Plot of *K* over time (top panel) for a simulation with a force of 5 pN applied between t=25 s and t=30 s (bottom panel). *K** denotes the outliers of *K* that emerge when the force is active.

To determine the K^* outliers from the K data, we used Tukey's fences[11] criterion based on the interquartile range IQR: any K value larger than the threshold value K_0 was considered an outlier, with K_0 given by

$K_0 = Q3 + q\ IQR,$

where Q3 is the third quartile of the distribution of K, and q is a positive number.

We explored the performance of the criterion for different values of q in numerical simulations, where the force patterns were known, to determine the best choice for q. We ran 40 simulations of 150 seconds with a total of 134 force events with random direction and localization. The magnitude, duration, and number of events per simulation were sampled from Poisson distributions with mean values: 2 pN, 3 seconds, and 3 events, respectively.

Supplementary Fig. S7 shows K distributions for three different simulations, alongside the outliers computed using q = 1 and q = 4. When q = 1, the method detects the outliers in K that correspond to the action of the forces (True Positives - TP), but it also spots outliers that do not align with times when a force is applied (False Positives - FP). Conversely, when q is increased to 4, the method becomes more precise at pointing out the application of forces when an outlier is detected. However, as the value of q increases, the method becomes less sensitive to the detection of forces and misses some events with undetected outliers (False Negatives - FN).

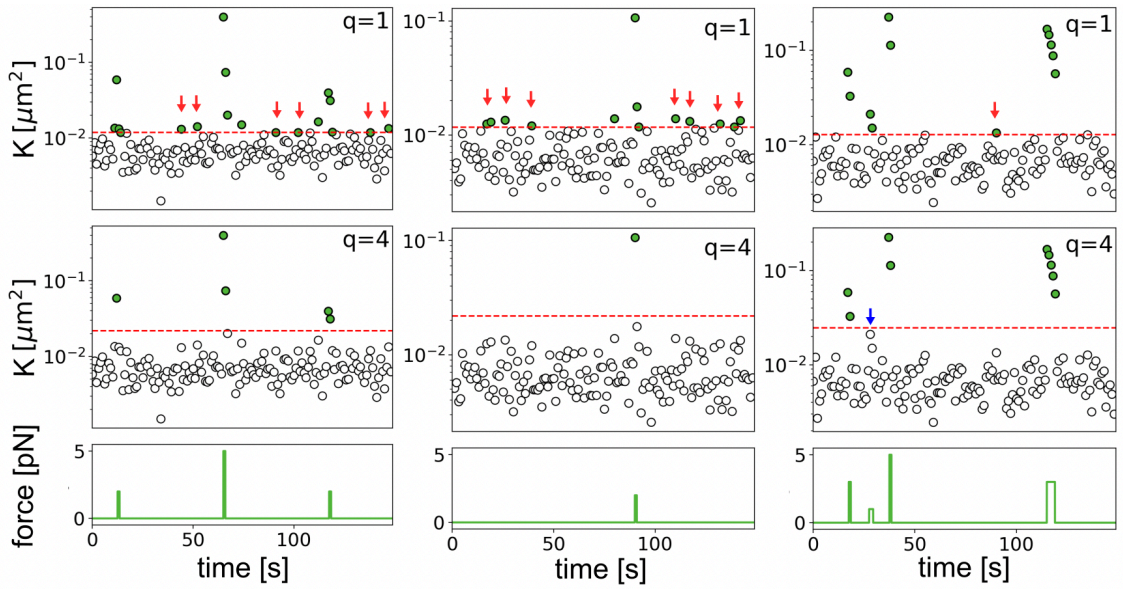

Supplementary Fig. S7: Outlier detection for different q. The columns represent data from three representative simulations, displaying K over time along with the corresponding K^* values (shown in green), calculated with q = 1 (top panel) or q = 4 (middle panel). Red arrows indicate instances where K^* does not coincide with periods of the force application (false detections). The blue arrow indicates an undetected outlier (false negative). The periods and magnitudes of the activated forces are displayed in the bottom row.

To evaluate the performance, we computed two magnitudes: Sensitivity -whether outliers were detected during periods of active forces- as:

$S = TP / (TP + FN)$

and False Discovery Rate -whether the detections correspond to actual periods of active forces:

$FDR = FP / (FP + TP)$.

Both magnitudes take values between 0 and 1. Supplementary Fig. S8 shows detections and false detections on the simulations based on different thresholds.

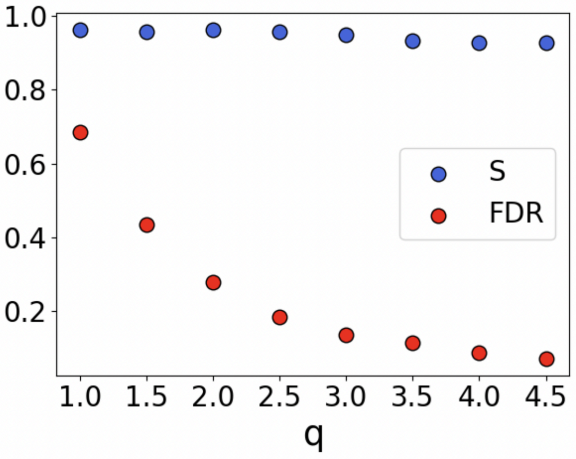

Supplementary Fig. S8: Performance evaluation of the force detection method with respect to *q*. Blue dots show the Sensitivity (S) of the method in detecting forces, while red dots show the False Discovery Rate (FDR).

Taking into account that the Sensitivity is almost constant for different values of *q,* while the False Discovery Rate decreases drastically as *q* increases, we decided to use $q = 4$ for the calculation of the threshold K_0.

b. Determination of events from the outliers' data

Figure S7 shows that, sometimes, more than one outlier is associated with the action of the same force. We want to group the outliers K^* in such a way that each group represents a single event. This will enable us to count the number of events (kicks) per trajectory.

Following an arbitrary criterion, we define that consecutive outliers are considered part of the same event. We also consider that two outliers, $K^*(t_1)$ *and* $K^*(t_2)$, are regarded as the same event if there is only one non-outlier, K, that separates them temporally. In other words, if the time difference between them is equal or less than two time steps Δt, they will be considered as a single event. Otherwise, they will be regarded as different events:

- $t_2 - t_1 \leq 2\Delta t \rightarrow$ *$K^*(t_1)$ and $K^*(t_2)$ are part of the same event*
- $t_2 - t_1 > 2\Delta t \rightarrow$ *$K^*(t_1)$ and $K^*(t_2)$ are different events*

Supplementary Fig. S9 illustrates this condition:

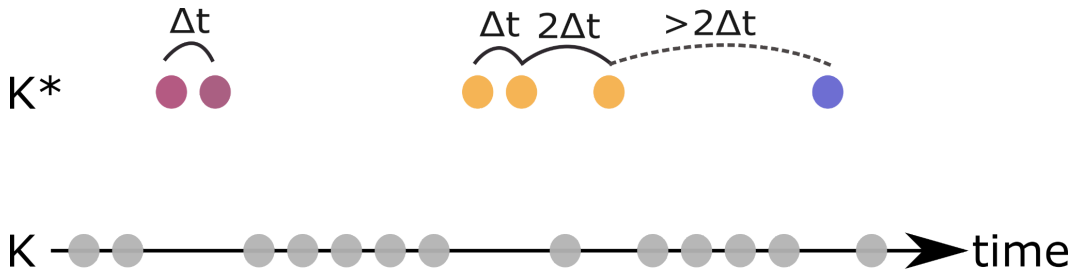

Supplementary Fig. S9. Schematic representation of the clustering criteria used to determine events. Outliers belonging to the same event are represented with the same color.

Finally, Supplementary Fig. S10 displays the events obtained from the analysis of the data shown in Supplementary Fig. S7, with q = 4.

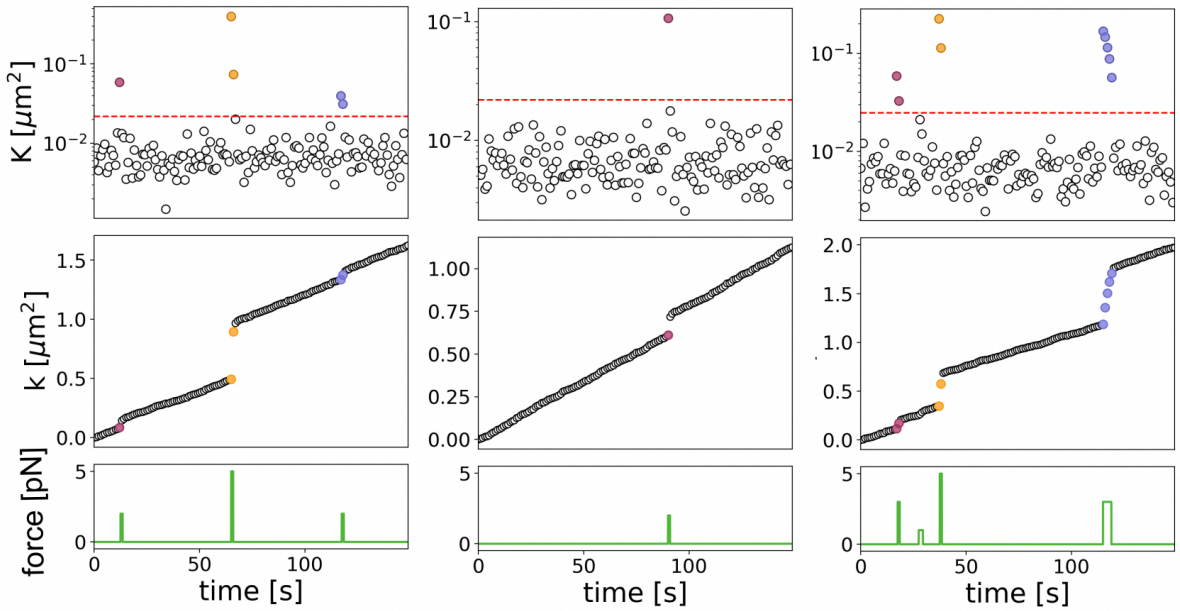

Supplementary Fig. S10: Events detection with q = 4. Each column of the panel represents data from the simulations shown in Supplementary Fig. S7. The top row shows *K* alongside the identified *K** events that are color-coded to indicate their association with a specific detected event using q = 4 and following the criterion illustrated in Supplementary Fig. S9. In the second row is the CSD with the same color coding applied to values that are deemed to belong to the same force application event. The periods and magnitudes of the active forces are displayed in the bottom row.

c. Distribution of the stationary values of *K*

We computed the median of *K(t)* for each trajectory as a robust estimate of the stationary (basal) values of *K*. Supplementary Fig. S11 shows the boxplot distribution of these median for each experimental condition.

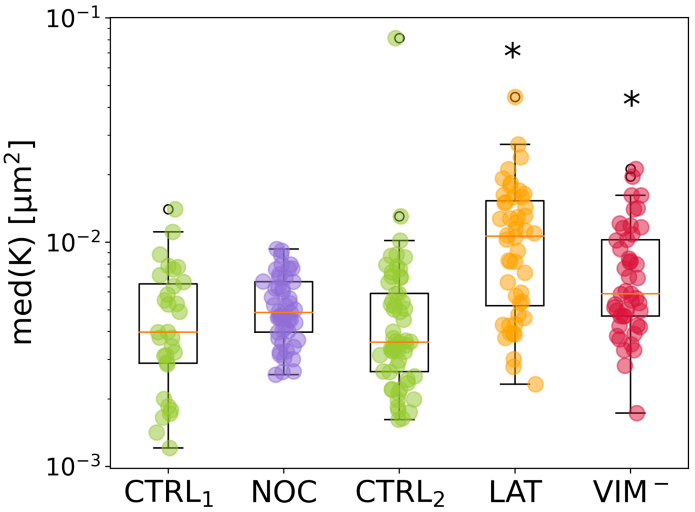

Supplementary Fig. S11: Median (med) of *K* values for each condition and sampling time (Table 1).

4. Description of Supplementary Videos

Supplementary Video S1: *X. laevis* melanocyte expressing EGFP-XTP (green: microtubules) and incubated with MitoTracker Deep Red FM (red: mitochondria) were imaged at 0.9 frames/s (190 frames) in CTRL condition. Pixel size: 0.103 µm. Related to Fig. 2a.

Supplementary Video S2: *X. laevis* melanocyte expressing EGFP-XTP (green: microtubules) and incubated with MitoTracker Deep Red FM (red: mitochondria) were imaged at 0.8 frames/s (100 frames) in VIM^- condition. Pixel size: 0.101 µm. Related to Fig. 2b, sub-diffusive example.

Supplementary Video S3: *X. laevis* melanocyte expressing EGFP-XTP (green: microtubules) and incubated with MitoTracker Deep Red FM (red: mitochondria) were imaged at 0.6 frames/s (140 frames) in NOC condition. Pixel size: 0.063 µm. Related to Fig. 2b, diffusive example.

Supplementary Video S4: *X. laevis* melanocyte expressing EGFP-XTP (green: microtubules) and incubated with MitoTracker Deep Red FM (red: mitochondria) were imaged at 0.6 frames/s (150 frames) in CTRL condition. Pixel size: 0.055 µm. Related to Fig. 2b, super-diffusive example, and Fig. 3b.

Supplementary Video S5: *X. laevis* melanocyte expressing EGFP-XTP (green: microtubules) and incubated with MitoTracker Deep Red FM (red: mitochondria) were imaged at 0.9 frames/s (150 frames) in CTRL condition. Pixel size: 0.063 µm. Related to Fig. 3a.

Supplementary Video S6: *X. laevis* melanocyte expressing EGFP-XTP (green: microtubules) and incubated with MitoTracker Deep Red FM (red: mitochondria) were imaged at 0.6 frames/s (100 frames) in NOC condition. Pixel size: 0.063 µm. Related to Fig. 3a.

Supplementary Video S7. *X. laevis* melanocyte expressing EGFP-XTP (green: microtubules) and incubated with MitoTracker Deep Red FM (red: mitochondria) were imaged at 0.90 frames/s (80 frames) in LAT condition. Pixel size: 0.103 µm. Related to Fig. 3a.

Supplementary Video S8: *X. laevis* melanocyte expressing EGFP-XTP (green: microtubules) and incubated with MitoTracker Deep Red FM (red: mitochondria) were imaged at 0.82 frames/s (120 frames) in VIM^- condition. Pixel size: 0.101 µm. Related to Fig. 3a.

5. References

[1] Gauger E. and H. Stark, Numerical study of a microscopic artificial swimmer, Phys. Rev. E 74, 021907 (2006).

[2] Monastra, A.G, M. F. Carusela, G. van der Velde, M. V. D'Angelo, and L. Bruno, Evolution of instabilities in filament buckling processes, Phys. Rev. E 99, 033004 (2019)

[3] Howard, J. Mechanics of Motor Proteins and the Cytoskeleton, Sinauer, Sunderland, MA, (2001).

[4] Volpe, G. and G. Volpe, Simulation of a Brownian particle in an optical trap, Am. J. Phys. 81, 224 (2013)

[5] Casafuz, A. B. F., De Rossi, M. C., & Bruno, L. Morphological fluctuations of individual mitochondria in living cells. *Journal of Physics: Condensed Matter*, *34*(9), 094005. (2021)

[6] Fernández Casafuz, A. B., De Rossi, M. C., & Bruno, L. Mitochondrial cellular organization and shape fluctuations are differentially modulated by cytoskeletal networks. *Scientific Reports*, *13*(1), 4065. (2023)

[7] Yamada, M. Yamaya, S. Okinaga, K. Nakayama, K. Sekizawa, S. Shibahara, and H. Sasaki, "Microsatellite polymorphism in the heme oxygenase-1 gene promoter is associated with susceptibility to emphysema," The American Journal of Human Genetics, vol. 66, no. 1, pp. 187–195, (2000)

[8] Wasserman, L. All of Statistics: A Concise Course in Statistical Inference. Springer-Verlag; New York: (2010)

[9] https://scikit-learn.org/stable/modules/mixture.html#gmm

[10] Schwarz G. Estimating the dimension of a model. Ann Stat.; 62:461–464(1978)

[11] Tukey, J. W. Exploratory data analysis (Vol. 2, pp. 131-160). Reading, MA: Addison-wesley. (1977)